Secretory trafficking maintains the organelle band for spindle separation during Arabidopsis meiosis

Ewa Weronika Piskorz[1, §], Yingrui Ma[1, §], Jun Yi[2], Maria Cuacos[1], David Kradolfer[2], Claudia Köhler[2, 3], Hua Jiang[1,4,*]

[1]Leibniz Institute of Plant Genetics and Crop Plant Research, Gatersleben 06466, Germany;
[2]Department of Plant Biology, Uppsala BioCenter, Linnean Center for Plant Biology, Swedish University of Agricultural Sciences, Uppsala, SE-75007, Sweden;
[3]Max Planck Institute of Molecular Plant Physiology, Potsdam-Golm, 14476, Germany;
[4]Institute for Biochemistry and Biology, University of Potsdam, Karl-Liebknecht-Str. 24-25, 14476 Potsdam-Golm, Germany
[§]These authors contributed equally.
*Corresponding authors: hua.jiang@uni-potsdam.de (Hua Jiang)

Abstract

Ploidy reduction is a critical aspect of meiosis, essential for the successful development of haploid germline cells. Notably, cellular processes during male meiosis vary between the major groups of flowering plants, with eudicots exhibiting simultaneous cytokinesis without an interkinesis phase, unlike monocots. Recent studies on the Arabidopsis *jason* (*jas*) mutant revealed that an organelle band plays a key role in spindle separation during simultaneous cytokinesis, though the mechanism is not fully understood. Here we identify a novel *jas* suppressor mutant, *peleus* (*pele*), which restores haploid pollen production in the *jas* background. PELE encodes a vacuole-localized protein that contributes to spindle separation by balancing the vacuolar pathway and secretory trafficking to the organelle band. JAS, PELE, and the ubiquitin-like protein UBQL coordinate the delivery of proteins and membrane components to the organelle band. Specifically, PELE and UBQL antagonistically fine-tune trafficking to the vacuole, while JAS adjusts the flow of secretory trafficking towards the organelle band. Our findings underscore the critical role of secretory trafficking in maintaining organelle band integrity and in ensuring precise spindle positioning during meiosis II. Our work provides novel insights into the regulation of the organelle band and spindle separation, enhancing our understanding of polyploidy generation in plants.

Introduction

Sexual reproduction, a fundamental process in plants, is essential for maintaining genetic diversity and facilitating plant adaptation to changing environments (McCormick 2004). Central to this process is meiosis, a specialized type of cell division that produces haploid gametes from diploid parental cells. During meiosis, chromosomes undergo recombination and segregation, ensuring ploidy reduction and the accurate distribution of genetic material to form haploid (1n) gametes. The process of meiosis in monocotyledonous plants typically involves successive cytokinesis, where reductional division is followed by the first cytoplasmic division, resulting in a "transitory dyad" with a cell wall separating the chromosome groups (De Storme and Geelen 2013). Subsequently, equational division occurs within each dyad cell, culminating in the formation of a tetrad of gametes. In dicotyledonous plants like *Arabidopsis thaliana* (Arabidopsis), cytokinesis is simultaneous, with a common cytokinetic event dividing the mother cell into four daughter cells at the end of telophase II (Rodkiewicz and Duda, 1988; Brown and Lemmon, 1996; Zhang et al., 2011). This type of cytokinesis requires organelles and vesicles to create a physical barrier known as the organelle band during meiosis II. The organelle band is crucial for preventing interactions between separated homologs and for ensuring proper segregation of sister chromatids by orienting meiotic spindles perpendicularly (Brownfield et al., 2015; Tchórzewska, 2017).

However, deviations from the standard course of meiosis lead to abnormal meiotic products, including unreduced (2n) gametes. Meiosis, particularly in males, occasionally yields 2n gametes with the same chromosome number as the parent cell, resulting in polyploidy (Brownfield and Köhler, 2011; De Storme and Geelen, 2013). Polyploidy is prevalent in plants and contributes to increased genetic diversity and adaptation. In specific Arabidopsis mutants, such as *jason* (*jas*) and *parallel spindle 1* (*ps1*), large quantities of viable, unreduced male gametes are produced due to the premature loss of the organelle band at prometaphase II or metaphase II, respectively (Brownfield et al., 2015; D'Erfurth et al., 2008; De Storme & Geelen, 2011; Erilova et al., 2009). Although the molecular basis of organelle band disruption is not fully understood, cytological analyses have revealed the presence of two meiotic spindles within the common cytoplasm during meiosis II, allowing unrestricted movement and abnormal orientations (Brownfield et al., 2015). Unreduced gametes play an important role in generating polyploids in nature and represent a promising breeding tool (Ramsey & Schemske, 1998; Adams & Wendel, 2005).

In this study, we explored the mechanism of spindle separation and unreduced gamete formation in Arabidopsis. Our recent study on the *jas* suppressor telamon (*tel*) demonstrated that enlarged meiocytes in *jas tel* mutants restored tetrad formation even in the absence of an organelle band, suggesting a link between cell size and spindle separation (Yi et al., 2023). Here, we analyzed another *jas* suppressor, *peleus* (*pele*), and found that it partially restored the organelle band in *jas* meiocytes, maintaining the distance between chromosome groups at metaphase II in male

meiocytes. Our findings further suggest that this restoration in *jas pele* mutants depends on secretory trafficking. We showed that PELE, the ubiquitin-like protein UBQL, and JAS work together to fine-tune the delivery of proteins and membrane components to the organelle band. This regulation occurs through a dual mechanism: (1) PELE and UBQL antagonistically control the secretory trafficking pathway to the vacuole, and (2) the interplay between UBQL-PELE and JAS further modulates the flow of secretory traffic toward either the organelle band or the vacuole. Together, these mechanisms precisely regulate the capacity of secretory trafficking to the organelle band, ensuring proper organelle band maintenance and accurate spindle separation during male meiosis II in Arabidopsis. These results reveal previously unknown roles for secretory trafficking in male meiosis and provide valuable insights into the regulation of the organelle band, spindle separation, and broader mechanisms contributing to polyploidy generation in plants.

Results

pele suppresses unreduced gamete formation

To investigate the genetic factors influencing unreduced gamete formation in plants, we conducted a forward genetic screen to identify suppressors of the *jas* mutation in Arabidopsis that forms a lot of 2n pollen. In this screen, we identified a mutant named *pele*, which in the *jas* background predominantly produced 1n pollen (Fig. 1A and 1B). This resulted in significantly decreased pollen grain size in *jas pele* compared to *jas* (Kolmogorov–Smirnov test, $P < 10^{-5}$) (Fig. 1B). The *jas* mutant exhibited 45% dyads and 33% triads, with all microspores from dyads and one-third from triads developing into 2n pollen. By contrast, the *jas pele* mutant showed significantly reduced numbers of triads and dyads (Chi-square test, $P < 10^{-5}$) (Fig. 1C and 1D), indicating that *pele* largely suppresses the male meiotic defect of the *jas* mutant.

Recently, we reported that the *tel* mutation suppressed 2n pollen formation within the *jas* background by augmenting the size of meiocytes (Yi et al., 2023). To test if *pele* and *tel* act in the same pathway, we combined them to generate the triple mutant *jas pele tel*. This combination led to a significant increase in the proportion of tetrads compared to the *jas pele* mutant (Chi-square test, $P < 10^{-5}$), implying that the mechanism by which *pele* suppresses 2n pollen formation is distinct from that of *tel* (Fig. 1E). Mutations in *OMISSION OF SECOND DIVISION 1* (*OSD1*) also cause unreduced gamete formation in Arabidopsis (d'Erfurth et al., 2008; d'Erfurth et al., 2009) by preventing chromatid separation in meiosis II. We investigated whether *pele* could also suppress the meiotic defect of the *osd1* mutant. The number of dyads and triads in *osd1 pele* double mutants did not substantially differ from those of the single mutants (Fig. 1E), indicating that *PELE* and *OSD1* act in different pathways. By contrast, *pele* significantly suppressed the male meiotic defect of the *ps1* mutant (Chi-square test, $P < 10^{-5}$). *ps1* produced 26% triads and 41.6% dyads, which decreased to 10.5% and 5.2%, respectively, in the *ps1 pele* mutant. Therefore, *pele*

103 suppressed unreduced gamete formation in *jas* and *ps1* mutants, both of which are related to
104 spindle separation during meiosis II.
105
106 **_pele_ rescues spindle separation in the _jas_ mutant**
107 The *jas* mutant has a defect in the separation of chromosome groups and spindles in meiosis II,
108 resulting in the formation of dyads and triads (Brownfield et al., 2015). Given that *pele* suppressed
109 the formation of abnormal meiotic products in the *jas* background, we examined whether the
110 separation of chromosome groups was recovered in *jas pele* by preparing chromosome spreads,
111 which allowed us to visualize chromosomes. The progression of male meiosis I was similar in the
112 wild type (WT), *jas*, and *jas pele* (Fig. 2A, left panel), which is consistent with the finding that *jas*
113 produces unreduced gametes during meiosis II. During male meiosis II in the WT, two
114 chromosome sets aligned at the cell equator, separated by the distinct organelle band. Sister
115 chromatids then segregated into four distal poles of the cell, where they decondensed into
116 haploid nuclei (Fig. 2A, right panel). In the *jas* mutant, the chromosomes became closed or fused,
117 leading to the formation of unreduced meiotic products (Fig. 2A, right panel). By contrast, in *jas*
118 *pele* during metaphase II, chromosome groups were separated, similar to the WT. Hence,
119 chromosome separation in meiosis II was recovered in *jas pele.*

120 The closed or fused chromosome groups in *jas* is associated with abnormal spindle positioning
121 (Brownfield et al., 2015). Therefore, we explored whether *jas pele* also restored spindle
122 positioning. To visualize meiotic spindles and determine their orientation, we used GFP-TUA6
123 marker lines in the WT, *jas*, and *jas pele* backgrounds. In the WT, meiotic spindles at metaphase
124 II positioned themselves perpendicularly (n = 89, Fig. 2B), which led to equal distribution of sister
125 chromatids into four newly forming daughter cells. By contrast, *jas* mutants in addition to
126 normally separated spindles (n = 43), displayed tripolar (n = 32) or fused spindles (n = 14), giving
127 rise to triads or dyads. However, *jas pele* mostly formed separated, perpendicular spindles, with
128 tripolar spindles constituting only 12.3% of detected conformations (n = 14 for a total of n = 114;
129 Fig. 2B), and no meiocytes contained fused spindles. We also observed the dynamics of spindle
130 positioning in WT, *jas*, and *jas pele*. In contrast to the stable, separated spindles in WT meiocytes
131 (Movie A), the spindles in *jas* were initially separated but soon became fused, which is in line with
132 the proposed function of JAS in maintaining the organelle band structure (Movie B, C). By
133 contrast, spindle separation was maintained during male meiosis in *jas pele* (Movie D), revealing
134 that *pele* rescued the defects in spindle positioning in the *jas* background.

135
136 **_pele_ partially rescues the organelle band**
137 Given that JAS functions to separate spindles by maintaining the structure of the organelle band,
138 we investigated whether this maintenance is rescued in *jas pele*. To better visualize the organelle
139 band and further test the effect of *pele*, we stained meiocytes in intact anthers with DAPI to avoid

140 removing the cytoplasm and thereby altering the 3-D structure of meiocytes in chromosome
141 spreads. Although DAPI primarily stains nuclear DNA, it also binds to mitochondrial DNA, meaning
142 the signal in the organelle band may partly reflect mitochondrial structures. Consistent with the
143 chromosome spreads, the DAPI-stained organelle band was well defined in the WT (Fig. 3A),
144 whereas it was partially or often completely absent in *jas*, while it became partially restored in
145 *jas pele* (Fig. 3B and 3C). We counted metaphase II meiocytes containing each type of the
146 organelle band. We considered the organelle band to be "partial" when more organelles were
147 detected between the chromosome sets than in the surrounding cytoplasm. Whereas 100% of
148 WT meiocytes contained complete bands, both *jas* and *jas pele* meiocytes exhibited only a partial
149 or absent organelle band. However, in *jas pele*, we detected partial bands in 58% of the cells (n =
150 82), whereas in *jas*, only a small subset of cells (15%, n = 106) contained partial bands (Fig. 3D).
151 The finding that nearly 60% of *jas pele* meiocytes contained a partial organelle band at metaphase
152 II could explain why this mutant produced 82% tetrads, as some meiocytes without an organelle
153 band were still able to undergo correct sister chromatid separation.

154 In addition to the localization of DAPI-stained organelles, we also observed markers of the plasma
155 membrane (PM) and the *trans*-Golgi network (TGN), which are concentrated in the organelle
156 band (Brownfield, Yi et al. 2015). While chromosome groups are fused in *jas* mutants, the
157 localization of the PM marker in *jas* was similar to wild type (WT) (n = 15 observed meiocytes for
158 jas, n = 8 for WT)) (Fig. 3E, left panel). Thus, disrupted spindle separation in *jas* mutants did not
159 appear to correlate with the localization of the PM marker. In contrast to its distribution in WT
160 (n=23 observed meiocytes), the TGN marker was dispersed in the cytoplasm of *jas* male meiocytes
161 (n=21) (Fig. 4E, right panel), which correlates with the dispersed DAPI-stained organelles and
162 disrupted organelle band. Therefore, we further examined the localization of the TGN marker in
163 *jas pele* mutants. Consistent with the partial recovery of the organelle band, chromosome groups
164 were separated by TGN marker-associated material (n=10 observed meiocytes), although not as
165 densely packed as in WT (Fig. 3E, right panel). Thus, the distribution of the TGN marker was
166 partially restored, coinciding with the partial recovery of the organelle band in *jas pele* mutants.

167 The partial recovery of the organelle band was confirmed by measuring the distance between
168 metaphase II chromosome sets. In *jas* mutants, chromosome sets were frequently either closer
169 than in WT or even touching (n = 106 observed meiocytes, Fig. 3F). In contrast, chromosome sets
170 in *jas pele* mutants were consistently located at a distance of at least 1.5 µm, significantly longer
171 than in *jas* mutants (Kolmogorov–Smirnov test, $P < 10^{-5}$) (Fig. 3F). Thus, the *pele* mutation
172 suppressed the *jas* phenotype by partially restoring organelle positioning and maintaining the
173 separation of chromosome sets at metaphase II.
174
175 **Vesicle trafficking maintains the organelle band in male meiocytes**

176 The organelle band consists of multiple types of organelles and vesicles, which are typically
177 associated with vesicle trafficking. Therefore, we investigated whether the restoration of the
178 organelle band in *jas pele* mutants depends on vesicle trafficking. If this is the case, inhibiting the
179 relevant trafficking pathways should diminish the rescue of the organelle band and tetrad
180 formation defect in *jas pele* mutants. To test this hypothesis, we examined the effects of vesicle
181 trafficking inhibitors on meiotic outcomes in *jas pele* mutants by treating inflorescences with
182 inhibitor solutions and assessing the meiotic products thereafter. Initially, we utilized
183 Concanamycin A, a chemical that impacts TGN function by blocking all TGN-associated pathways,
184 including the endocytic and the secretory trafficking pathways (Dettmer et al., 2006; Reichardt et
185 al., 2007). This treatment notably weakened the suppressive effect of *pele* on the *jas* mutant
186 phenotype (Chi-square test, $P < 10^{-5}$), leading to a significant increase in the percentage of dyads
187 and triads from ~30% (treated with DMSO) to ~70% (Chi-square test, $P < 10^{-5}$) (Fig. 4A). This
188 suggests that *pele* indeed restores spindle separation through its effect on vesicle trafficking.

189 To further investigate which specific pathway *pele* affects, we treated inflorescences with
190 Wortmannin and Brefeldin A (BFA), which inhibit the endocytic pathway and the secretory or
191 recycling pathways, respectively. While Wortmannin did not affect the phenotype of *jas pele*
192 mutants (Fig. 4A), BFA significantly increased the percentage of triads and dyads (to ~60%) (Chi-
193 square test, $P < 10^{-5}$). Furthermore, to verify the influence of the inhibitor treatment on organelle
194 band recovery, we assessed the percentage of the partial organelle band. Consistent with the
195 tetrad formation results, BFA treatment suppressed the partial organelle band in *jas pele* mutants
196 (Chi-square test, $P < 10^{-5}$), whereas Wortmannin did not (Fig. 4B). Consequently, BFA, but not
197 Wortmannin, significantly reduced the distance between two groups of chromosomes at
198 metaphase II (Kolmogorov-Smirnov, $P < 0.01$) (Fig. 4C).

199 While treatment with Concanamycin A and BFA notably induced the production of abnormal
200 meiotic products in *jas pele* mutants, these chemicals had no effect on male meiosis in WT plants,
201 suggesting that vesicle trafficking partially contributes to maintain the organelle band in WT
202 plants and that another mechanism independently stabilizes the organelle band, unrelated to
203 vesicle trafficking.
204
205 ***PELE* encodes a vacuole-localized protein**
206 To identify *PELE*, we map-based cloned *pele* and identified a C-to-T substitution in the 18th exon
207 of the gene AT5G11700. This substitution caused a tryptophan to be replaced by a stop codon.
208 Derived cleaved amplified polymorphic sequence (dCAPS) analysis and Sanger sequencing
209 performed on *jas* and *jas pele* DNA confirmed that the substituted nucleotide originated from
210 ethyl methanesulfonate (EMS) treatment (Fig. S1A and B).

211 To further test whether AT5G11700 is the *PELE* gene, we crossed the at5g11700 T-DNA insertional
212 mutant with *jas* and examined the double mutant progeny in the F_2 generation. The double
213 mutants exhibited a phenotype similar to *jas pele*, producing approximately 80% tetrads (Fig.
214 S1C). To verify this, we generated a construct containing the WT genomic AT5G11700 sequence
215 along with its 1.5-kb promoter and used this construct to transform *jas pele* plants. AT5G11700
216 complemented the *jas pele* phenotypes in the T_1 and T_2 generations, restoring 1n pollen
217 formation and increasing the number of dyads (Table S1). Thus, we identified *PELE* as AT5G11700.

218 To elucidate the role of PELE in meiosis, we crossed *jas pele* with WT and obtained the *pele* single
219 mutant. Analysis of pollen size indicated that *pele* produced uniformly haploid pollen (Fig. S2A),
220 which developed from the reduced meiotic products (97.8% tetrads, n = 458, Fig. S2B). Moreover,
221 we performed chromosome spreads of the single mutant. At metaphase II, two chromosome sets
222 were separated by a complete organelle band characteristic of the WT (Fig. S2C), and no other
223 meiotic abnormalities were detected. Hence, the *pele* mutation affects meiotic progression only
224 in the presence of the *jas* or *ps1* mutation.

225 PELE consists of 1,453 amino acids and lacks known domains that could suggest its biological
226 function. Online sources, such as SMART (embl-heidelberg.de), predicted the presence of a signal
227 peptide at its N terminus and at least four transmembrane domains (Fig. S3A), indicating that it is
228 a membrane-localized protein. Previous studies localized PELE to the vacuole membrane and
229 annotated it as a putative multi-transmembrane tonoplast protein of unknown function (Endler
230 et al., 2006; Shimaoka et al., 2004). To examine the *PELE* expression pattern, we fused the *PELE*
231 promoter and genomic sequence with the *β-GLUCURONIDASE* (*GUS*) gene, transformed this
232 construct into WT plants, and subjected the progeny of the resulting transformants to GUS
233 staining. The *PELE* promoter was nearly constitutively expressed in all plant organs, including
234 roots (Fig. S3B, C), rosette leaves (Fig. S3D), cauline leaves (Fig. S3E), and inflorescences (Fig. S3F),
235 throughout all stages of plant development.

236 We further observed PELE-GFP localization in male meiocytes by fusing the *PELE* promoter and
237 genomic sequence with GFP. PELE-GFP was dispersed in the cytoplasm of male meiocytes (Fig.
238 5A), partially overlapped with the area of the organelle band, suggesting the functional
239 relationship between PELE and the regulation of organelle band. In contrast to the pattern in male
240 meiocytes, in roots, we observed co-localization of PELE-GFP with markers for the late
241 endosome/prevacuolar compartment and the tonoplast but not with other markers (Fig. 5B, Fig.
242 S4, Table S2). Moreover, PELE-GFP formed vesicle-like structures that emitted bright florescence
243 that, however, did not co-localize with any of the Wave line markers for the ER, Golgi, TGN/early
244 endosomal compartments or PM (Fig. S4), indicating that PELE-GFP was localized at other types of
245 organelles or aggregated in cytoplasm. In summary, PELE localizes in the late endosome and
246 tonoplast in root cells, consistent with its functional role in vesicle trafficking during male meiosis.

247

248 **UBQL together with PELE fine-tune secretory trafficking to the organelle band**

249 Pharmacological and genetic analyses suggest that secretory pathways are crucial for regulating
250 the organelle band. The tonoplast localization of PELE-GFP indicates its role in this process. Since
251 the *pele* mutation rescues defects in secretory trafficking, we propose that PELE helps balance
252 vacuolar and secretory pathways. This mutation may reroute cargoes that would normally go to
253 the vacuole toward the organelle band, potentially explaining the partial rescue of the *jas*
254 phenotype. To understand how PELE influences this process, we investigated potential PELE
255 interactors. Through the BioGRID protein interaction database (Oughtred et al., 2019), we
256 identified UBQL (AT5G42220), a ubiquitin-like protein, as a potential candidate. Consistent with
257 this, AlphaFold2 predictions indicated an interaction between PELE and UBQL, specifically
258 through amino acids W^{1028}, R^{1029}, and G^{1031} of PELE, and E^{758}, Q^{753}, and G^{766} of UBQL (Fig. 6A and
259 6B). We validated this interaction through a split-ubiquitin yeast two-hybrid assay. Since full-
260 length PELE inhibited yeast growth, we tested a fragment of PELE ($PELE^{909-1296}$), which includes
261 the predicted interaction sites. In addition to testing UBQL and $PELE^{909-1296}$, we included UBQL
262 with an empty vector as a negative control and UBQL with Nub1 as a positive control. The yeast
263 containing UBQL and $PELE^{909-1296}$ showed growth similar to the positive control, with noticeably
264 more colonies compared to the negative control. Thus, our findings support an interaction
265 between UBQL and PELE in yeast consistent with an interaction predicted by *in silico* analyses.

266

267 To further investigate the role of UBQL in secretory trafficking-mediated spindle separation, we
268 crossed *jas pele* with *ubql* to generate *jas ubql* and *jas pele ubql* mutants. Despite the interaction
269 between UBQL and PELE, the *ubql* mutation significantly increased the production of dyads under
270 the *jas* background (Chi-square test, $P < 10^{-5}$) (Fig. 6D). This suggests that UBQL positively affects
271 secretory trafficking, in contrast to PELE, which may negatively affect the process potentially due
272 to a primary role in the vacuolar pathway. Given these opposing roles, we hypothesized that
273 mutating both PELE and UBQL in the *jas* background would neutralize their individual effects,
274 leading to levels of dyads and triads in the *jas pele ubql* mutant similar to in the *jas* mutant. As
275 expected, the percentage of dyads in *jas pele ubql was* significantly lower than in *jas pele*, making
276 it closer to the levels observed in *jas* mutants (Fig. 6D). Each triad produces one diploid (2n) pollen
277 and two haploid (1n) pollen, while each dyad generates two 2n pollen. Based on these patterns,
278 we speculated on the proportions of 1n and 2n pollen from the tetrad analysis (Fig. 6E). As
279 anticipated, the percentage of diploid pollen changed significantly when *PELE* and *UBQL* were
280 mutated individually in the *jas* background (Chi-square test, $P < 10^{-5}$). However, no significant
281 difference was found between *jas* and *jas pele ubql*, suggesting a balancing effect when both *PELE*
282 and *UBQL* are disrupted as both the vacuolar and the secretory pathway may be affected by the
283 respective mutants. In line with the tetrad and pollen analysis results, chromosome distance at

284 metaphase II was comparable between *jas* and *jas pele ubql*, whereas the distance was shorter in
285 *jas pele ubql* than in *jas pele* (Fig. 5F). These findings strongly support the conclusion that UBQL
286 and PELE antagonistically fine-tune secretory trafficking to the organelle band, where UBQL takes
287 over a positive function in contrast to PELE that negatively affects the process.
288
289 **Discussion**
290 Our findings highlight the function of secretory trafficking in maintaining the integrity of the
291 organelle band during male meiosis in Arabidopsis. Previous data revealed localization of JAS to
292 the organelle band and its association with various organelles in root cells, suggesting that JAS is
293 involved in organelle band maintenance (Brownfield et al., 2015; Cabout et al., 2017). Here, we
294 identified PELE as factor negatively impacting organelle band formation or maintenance. We
295 show that mutations of *PELE* restore the organelle band in the *jas* mutant background. This
296 restored organelle band in *jas pele* is disrupted by inhibiting secretory trafficking. PELE is
297 associated with the tonoplast in root cells, consistent with a possible function in vacuolar vesicle
298 trafficking. Unlike the significant effects on organelle band formation observed in the *jas* and
299 restored in the *jas pele* mutant, none of the chemical treatments with vesicle trafficking inhibitors
300 on their own disrupted organelle band formation and spindle separation in WT plants. This may
301 suggest the existence of another mechanism independent of vesicle trafficking that stabilizes the
302 organelle band. Considering the substantial disruption of the organelle band in the *jas* mutant,
303 we propose that JAS is responsible for both, secretory trafficking-dependent and independent
304 mechanisms. Therefore, in the *jas pele* mutant, restored secretory trafficking resulted in a partial
305 organelle band, while inhibition of vesicle trafficking suppressed the organelle band. In future
306 studies, exploring the nature of the secretory trafficking-independent mechanism in organelle
307 band formation promises to yield intriguing insights.
308
309 Secretory trafficking typically delivers proteins to the plasma membrane or vacuole (Zhang et al.
310 2019). However, during cytokinesis, it is redirected towards the zone where the future cell plate
311 will form (Kanazawa and Ueda 2017). The enrichment of the plasma membrane marker PIP1;4 in
312 the organelle band at metaphase II (Brownfield et al., 2015) suggests a similar redirection of
313 vesicle trafficking to the central zone of male meiocytes in Arabidopsis. Notably, treatment with
314 BFA, an inhibitor of ER-to-Golgi transport, suppressed the rescued spindle separation observed in
315 *jas pele* mutants, indicating that the secretory pathway, including ER-to-Golgi transport, is
316 involved in organelle band regulation. Interestingly, the effect of BFA treatment in male
317 meiocytes differed from its effect in seedlings, where the functional redundancy between the
318 BFA-sensitive GNOM and the BFA-resistant GNL1 limits the observable impact of BFA (Van
319 Damme et al., 2008). In male meiocytes, however, the effect of BFA was already evident in the
320 wild-type background, suggesting that GNL1 does not compensate for GNOM in ER-to-Golgi
321 transport during male meiosis, unlike in seedlings.
322

323 Wortmannin treatment did not produce a significant effect on *jas pele*, suggesting a minor role of
324 endocytic transport in organelle band regulation. The localization of the endomembrane marker
325 PIP1;4, which is likely transported via endocytic transport, remains unaffected when the organelle
326 band is disrupted in *jas*, supporting the notion that the import of endomembrane-localized
327 proteins alone is insufficient to maintain the organelle band structure. However, we cannot
328 entirely rule out the involvement of the endocytic pathway in organelle band regulation, as
329 Wortmannin does not completely inhibit endocytosis, leaving open the possibility that endocytic
330 vesicles contribute to this process (Leshem et al. 2007). Therefore, the relative contributions
331 between secretory and endocytic trafficking to organelle band regulation remain to be further
332 determined.
333
334 The transport of newly synthesized proteins and membrane components to the plasma
335 membrane or vacuole is tightly regulated during plant development (Zhang et al., 2019). PELE is
336 primarily localized in late endosomes and the tonoplast in root cells, suggesting a similar role in
337 male meiocytes, although the vacuole morphology is altered. During somatic cytokinesis,
338 vacuoles undergo substantial changes in organization, size, and volume, with an 80% reduction in
339 vacuole volume compared to prometaphase cells (Segui-Simarro and Staehelin, 2006). Similar
340 dynamics may occur in male meiocytes, potentially altering the localization and function of PELE
341 compared to root cells. At metaphase II, as a tonoplast-localized protein, PELE is likely primarily
342 involved in transport to or at the tomoplast, while JAS is required for secretory trafficking toward
343 the organelle band. To modulate the activity of PELE, UBQL antagonizes PELE by blocking
344 secretory transport to the vacuole. On the other hand, *pele* mutations may reroute transport of
345 some cargoes to the vacuole into the secretory pathway contributing to partial restoration of the
346 organelle band. Potentially antagonistic roles of PELE and UBQL thus may help fine-tune the
347 capacity of secretory trafficking to the vacuole (Fig. 7) and to the PM/organelle band, balancing
348 the two pathways. In *jas male* meiocytes, excessive vacuolar trafficking disrupts the organelle
349 band, but in *jas pele* mutants, UBQL partially rescues band function by restoring some trafficking
350 to the organelle band. In *jas ubql* mutants, the absence of UBQL enhances the ability of PELE to
351 reroute trafficking to the vacuole, worsening organelle band disorganization and affecting spindle
352 separation. This secretory trafficking is fine-tuned by two mechanisms: PELE and UBQL balance
353 vacuolar transport, and their interplay with JAS regulates trafficking to the organelle band,
354 ensuring proper spindle separation during male meiosis II in Arabidopsis.
355
356 The resemblance of the organelle band to the cytokinesis-derived cell plate formed during
357 successive cytokinesis raises questions about the connection between organelle band formation
358 and cytokinesis. Whereas vesicle trafficking, particularly exocytosis, is essential for cell plate
359 formation during cytokinesis (Reichardt et al., 2007), successful cell plate formation does not
360 occur in male meiocytes with simultaneous cytokinesis (De Storme and Geelen, 2013). To ensure
361 proper spindle separation during male meiosis II, plants may have evolved unique mechanisms

involving vesicle trafficking to maintain organelles in a band between spindles, a process likely dependent on JAS. The specificity of JAS to eudicots (Cabout et al., 2017), with monocots using a different mechanism during meiosis II, highlights the diverse regulatory pathways involved in plant reproduction. Together, our results generate novel insight into the role of secretory trafficking in maintaining the organelle band, allowing proper spindle separation during simultaneous cytokinesis.

Materials and Methods

Plant materials and growth conditions

Seeds of the Arabidopsis (*Arabidopsis thaliana*) T-DNA insertional mutants *peleus* (SALK_209914C), the *jas-3* allele (SAIL_813_H03), and the *ps1-1* allele (SALK_078818) were obtained from the Nottingham Arabidopsis Stock Centre (NASC). The marker lines of organelles from the Wave line collection harboring endomembrane system markers fused with mCherry (Geldner et al., 2009) were obtained from NASC. The WT Arabidopsis ecotype Col-0 was employed.

Seeds were stratified for 48 hours at 4°C in water in the dark, sown in soil, and propagated in a phytotron under a 16-h-light/8-h-dark photoperiod. The temperature was set to 22°C in the daytime and 19°C at night, the light intensity was 115 $\mu mol \cdot m^{-2} \cdot s^{-1}$, and the relative humidity was 70%.

EMS mutagenesis of *jas-3* seeds, genetic mapping, sequencing, and mutant identification were carried out as previously described (Kradolfer et al., 2013; Yi et al., 2023).

Pollen phenotyping

To measure pollen size, a drop of 1× PBS with 0.1% Triton X-100 was placed on a microscope slide and two to three open flowers were dipped into the solution to release pollen. After covering the sample with a coverslip, the pollen was imaged at 10× magnification under a SMZ1500 Nikon optical microscope. The size of each pollen grain was measured in ImageJ using a self-made algorithm, in which the 'Area' category reflects the 2-D area of a pollen grain.

Cytological analysis

To count the meiotic products, whole inflorescences were fixed in Carnoy's fixative (ethanol:acetic acid 3:1) for at least 3 h at room temperature. After two washes with 1× PBS, two to three of the largest white buds were dissected under a stereoscope, and the anthers were cut into pieces using sharp needles or a razorblade. The meiotic products were stained with 0.1–0.2% toluidine blue solution, viewed at 10× magnification under a stereoscope, and manually counted.

397 Chromosome spreads were prepared by fixing the inflorescences in Carnoy's fixative. Two to
398 three ca. 0.5 mm long white buds were separated from the rest of the buds and digested for 20
399 min at 37°C in 10 mM sodium citrate buffer, pH 4.5, with 0.3% cellulase and 0.3% pectinase. The
400 buds were washed tree times in 1× PBS and placed on a slide under a stereoscope. The meiotic
401 anthers were released and macerated with sharp tweezers. The homogenous suspension of cells
402 was quickly incubated in 60% acetic acid on a hot plate set to 45°C, gently spread on a slide, and
403 washed with a drop of fresh, ice-cold Carnoy's fixative. The slide was left to dry and covered with
404 2 µm/mL DAPI (Roth) in antifade solution. Meiocytes were examined using a Zeiss Axioplan 2
405 fluorescence microscope equipped with a Plan-Apochromat 63x/1.40 oil immersion objective.

406 Whole meiotic anthers were analyzed by fixing inflorescences undergoing meiosis in Carnoy's
407 fixative as previously described and removing intact anthers from the meiotic buds. The anthers
408 were incubated in DAPI buffer (0.4 µL of 2 µg/mL DAPI in 1× PBS + 0.15% Triton X-100) for at least
409 20 min at room temperature in the dark. The samples were sealed under a coverslip and imaged
410 using a Zeiss LSM780 confocal microscope (Carl Zeiss, Jena, Germany) with a C-Apochromat
411 40x/NA 1.2 water immersion objective and DAPI filter.

412 To visualize various cellular components fused with fluorescent tags, inflorescences undergoing
413 meiosis were fixed in 100% methanol at –20°C for 20 min. The samples were washed with ice-
414 cold 1× PBS and kept on ice until processing. Intact meiotic anthers were prepared for analysis
415 using the 'whole anther analysis' procedure, with occasional dissecting using a razorblade or
416 gentle squashing with a coverslip to enhance weak signals. Imaging was performed using a Zeiss
417 LSM780 confocal microscope equipped with a C-Apochromat 40x/NA 1.2 water immersion
418 objective. The DAPI filter was used for imaging chromosomes and the organelle band, eGFP for
419 meiotic spindles and PELE-GFP, and mCherry for endomembrane system marker lines.

420

421 **Inflorescence culture and inhibitor treatment**

422 The main stems of 6-week-old Arabidopsis inflorescences were cultured on medium comprising
423 200 mL of 1× MS salts, 3% sucrose (w/v), and 1× vitamins (Feldmann, 1991). The pH was adjusted
424 to 6.0 with KOH, and the medium was autoclaved at 121°C for 15 minutes prior to use. Inhibitors
425 were prepared as a master mix. Concanamycin A (ChemCruz) powder was dissolved in DMSO to
426 create a 200 µM stock solution. Wortmannin (Abcam) powder was dissolved in DMSO to generate
427 a 3 mM stock solution. Both solutions were stored at –20°C and fully dissolved before the
428 experiment. Brefeldin A solution 1000× (BioLegend) was freshly diluted in 9× DMSO to create the
429 master mix prior to use. The treatment medium was prepared by adding master mix to the
430 inflorescence culture medium at a ratio of 1:100, resulting in a final concentration of 2 µM
431 Concanamycin A, 30 µM Wortmannin, and 7 µM Brefeldin A. The prepared treatment medium
432 was aliquoted into 0.5-mL Eppendorf tubes and sealed with a sheet of adhesive foil to prevent

433 contamination. A needle was used to create a hole in the middle of each tube. Inflorescences in
434 excellent condition were selected, carefully cut with a blade, and immediately inserted into the
435 hole in each 0.5-mL Eppendorf tube for treatment. The culture system was incubated under
436 standard conditions for 22 h. After this incubation period, the treated inflorescences were fixed
437 and analyzed. The fixed samples were stored at a maximum of 4°C for up to 1 week.
438
439 **Lightsheet Fluorescence Microscopy**
440 Lightsheet Flurescence Microscopy (LSFM) was performed using a Lightsheet 7 (Carl Zeiss GmbH)
441 equipped with two pco.edge 4.2 sCMOS cameras (PCO AG) according to previous reports (Ovecka
442 et al. 2015, Valuchova et al. 2020, Feng et al. 2023) with minor modifications. ~0.5 mm
443 Arabidopsis flower buds were carefully detached from the inflorescence, dissected to remove
444 outer sepals, and inserted into 1.5 mm (inner diameter) glass capillaries (size 3, green mark; Carl
445 Zeiss GmbH, 701908) containing 1% low melting agarose (Sigma-Aldrich, A9045) prepared in
446 distilled water. Once fitted in the microscope, the agarose cylinder containing the sample was
447 extruded into the imaging chamber filled with distilled water. Temperature in the chamber was
448 set to 21 °C, and no artificial light source was supplemented. Imaging was done with 20x (W Plan-
449 Apochromat 20x/1.0) detection and 10x (LSFM 10x/0.2 foc) illumination objectives and 2.0x
450 zoom. Excitation was done with 0.8% 488 nm laser line. Dual-side illumination was chosen, and
451 pivot scan was turned on to reduce shadowing. Z-stacks covering the whole anther were taken
452 every 45 sec. Images were acquired with ZEN Black 3.1, and processing (selection of single z-stack,
453 drift correction where needed, ROI selection, movie export) was done with ZEN Blue 3.4 (both
454 from Carl Zeiss GmbH).
455
456 **DNA library preparation**
457 The leaves of 3-week-old seedlings were snap-frozen and stored in –80°C until DNA extraction.
458 The leaves were pooled and homogenized using a mortar and pestle. DNA was extracted from the
459 sample using a DNeasy Plant Mini Kit from Qiagen according to the manufacturer's protocol. Four
460 micrograms of high-quality DNA was sonicated with a Bioruptor (Diagenode) into 200- to 300-bp
461 fragments, and the DNA library was prepared using a VAHTS Universal DNA Library Prep Kit for
462 Illumina from Vazyme according to the manufacturer's protocol. The concentration of the
463 libraries was measured on a Qubit Fluorometer (Thermo Fisher Scientific), and library quality was
464 measured on an Agilent 2100 Bioanalyzer (Agilent Technologies). The libraries were sequenced
465 at Novogene, UK, and at least 15 million reads were produced for each sample (*jas pele* and *jas*
466 as a control). Reads were mapped to TAIR10 Col-0 genomes with HISAT2 (Kim et al., 2019).
467
468 **Plasmid construction and genotyping**

469 To generate the genomic *PELEUS* (*PELE*) construct for complementation analysis, a 10,590-bp
470 fragment of AT5G11700, including 1,531 bp of the upstream region, the stop codon, and 570 bp
471 of the downstream region, was amplified from Col-0 genomic DNA with Phanta Max Super-
472 Fidelity DNA Polymerase from Vazyme (forward primer 5'-
473 ATAAGCTTGATATCGAATTCttggaatccgcgaaaatgttatg-3' and reverse primer 5'-
474 ACTAGTGGATCCCCCGGGgaaggggaagatgagggaatga-3'). The TSK108 entry vector was linearized
475 with *Eco*RI and *Sma*I (ThermoFisher), and the g*PELE* fragment was inserted into the vector using
476 a ClonExpress Ultra One Step Cloning Kit (Vazyme). To generate the gPELE-eGFP and gPELE-GUS
477 constructs, the same genomic locus, but without the stop codon and the downstream region, was
478 amplified and cloned as described (reverse primer 5'-
479 ACTAGTGGATCCCCCGGGCGACTGCCAAAACAGCTCAT-3'). The assembled sequences were
480 transferred into Gateway-compatible destination vectors using LR Clonase (ThermoFisher): PELE
481 into pGWB510, PELE-GFP into pH7FWG;0, and PELE-GUS into pGWB533. After verifying the
482 constructs by Sanger sequencing, Arabidopsis plants were transformed with the vectors using the
483 floral dip method (Bent & Clough, 1998) mediated by *Agrobacterium tumefaciens* strain GV3101.
484 Transgenic lines were selected on ½ MS plates supplemented with 35 µg/mL hygromycin.

485 To genotype the mutants and transformants, DNA was extracted from 3-week-old plants using
486 the Edwards method (200 mM Tris-HCl pH 7.5, 250 mM NaCl, 25 mM EDTA, and 0.5% SDS)
487 (Edwards et al., 1991) with some modifications, and PCR was carried out with 2× Taq Master Mix
488 from Vazyme. Primers used for genotyping are listed in Table S2.
489
490 **GUS staining**
491 WT Col-0 plants were transformed with pGWB533-PELE-GUS, and the resulting seeds were
492 selected on ½ MS plates supplemented with 35 µg/mL hygromycin before being transferred to
493 soil at approximately 2 weeks after germination. Various organs of the positive transformants
494 were collected at different developmental stages, stained with GUS staining solution (50 mM
495 phosphate buffer, 10 mM EDTA, 0.1% Triton X-100, 1 mM potassium ferricyanide III, 1 mM
496 potassium ferrocyanide II, and 1 mg/mL X-Gluc), incubated overnight at 37°C in the dark, and
497 washed with 70% ethanol; WT Col-0 was used as a negative control.
498
499

500 **References**

501 **Adams, K. L., & Wendel, J. F.** (2005). Polyploidy and genome evolution in plants. *Current*
502 *Opinion in Plant Biology*, *8*(2), 135–141. https://doi.org/10.1016/j.pbi.2005.01.001
503 **Bent, A. F., & Clough, S. J.** (1998). Floral dip: a simplified method for Agrobacterium-mediated
504 transformation of Arabidopsis thaliana. *Plant Journal*, *16*(6), 735–743.
505 **Brown, R.C., Lemmon, B.E.** (1996). Nuclear cytoplasmic domains, microtubules and organelles
506 in microsporocytes of the slipper orchid Cypripedium californicum A. Gray dividing by
507 simultaneous cytokinesis. Sex Plant Reprod 9: 145–152
508 **Brownfield, L., & Köhler, C.** (2011). Unreduced gamete formation in plants: Mechanisms and
509 prospects. *Journal of Experimental Botany*, *62*(5), 1659–1668.
510 https://doi.org/10.1093/jxb/erq371
511 **Brownfield, L., Yi, J., Jiang, H., Minina, E. A., Twell, D., & Köhler, C.** (2015). Organelles maintain
512 spindle position in plant meiosis. *Nature Communications*, *6*.
513 https://doi.org/10.1038/ncomms7492
514 **Cromer, L., Heyman, J., Touati, S., Harashima, H., Araou, E., Girard, C., Horlow, C., Wassmann,**
515 **K., Schnittger, A., de Veylder, L., & Mercier, R.** (2012). OSD1 promotes meiotic progression
516 via APC/C inhibition and forms a regulatory network with TDM and CYCA1;2/TAM. *PLoS*
517 *Genetics*, *8*(7). https://doi.org/10.1371/journal.pgen.1002865
518 **Cui, Y., Zhao, Q., Gao, C., Ding, Y., Zeng, Y., Ueda, T., Nakano, A., & Jiang, L.** (2014). Activation
519 of the Rab7 GTPase by the MON1-CCZ1 complex is essential for PVC-to-vacuole trafficking
520 and plant growth in Arabidopsis. *Plant Cell*, *26*(5), 2080–2097.
521 https://doi.org/10.1105/tpc.114.123141
522 **D'Erfurth, I., Jolivet, S., Froger, N., Catrice, O., Novatchkova, M., Simon, M., Jenczewski, E., &**
523 **Mercier, R.** (2008). Mutations in AtPS1 (Arabidopsis thaliana Parallel Spindle 1) lead to the
524 production of diploid pollen grains. *PLoS Genetics*, *4*(11), 1–9.
525 https://doi.org/10.1371/journal.pgen.1000274
526 **Dawe, R. K.** (1998). Meiotic chromosome organization and segregation in plants. *Annual Review*
527 *of Plant Biology*, *49*, 371–395. https://doi.org/10.1146/annurev.arplant.49.1.371
528 **De Storme, N., & Geelen, D.** (2011). The arabidopsis mutant jason produces unreduced first
529 division restitution male gametes through a parallel/ fused spindle mechanism in meiosis II.
530 *Plant Physiology*, *155*(3), 1403–1415. https://doi.org/10.1104/pp.110.170415
531 **De Storme, N., & Geelen, D.** (2013). Cytokinesis in plant male meiosis. *Plant Signaling and*
532 *Behavior*, *8*(3). https://doi.org/10.4161/psb.23394
533 **De Storme, N., & Geelen, D.** (2020). High temperatures alter cross-over distribution and induce
534 male meiotic restitution in Arabidopsis thaliana. *Communications Biology*, *3*(1), 1–15.
535 https://doi.org/10.1038/s42003-020-0897-1

536

537 **Dettmer J, Hong-Hermesdorf A, Stierhof YD, Schumacher K.** (2006). Vacuolar H+-ATPase
538 activity is required for endocytic and secretory trafficking in Arabidopsis. *Plant Cell*, 18,
539 715-730.
540 **Doyle, S.M., Haeger, A., Vain, T., Rigal, A., Viotti, C., Langowska, M., Ma, Q., Friml, J., Raikhel,**
541 **N.V., Hicks, G.R.** (2015). An early secretory pathway mediated by GNOM-LIKE 1 and GNOM
542 is essential for basal polarity establishment in Arabidopsis thaliana. *Proc Natl Acad Sci U S A*
543 **112**: E806-815
544 **Edwards, K., Johnstone, C., & Thompson, C.** (1991). A simple and rapid method for the
545 preparation of plant genomic DNA for PCR analysis. *Nucleic Acids Research*, *19*(6), 1349.
546 https://doi.org/10.13031/aim.20141900217
547 **Endler, A., Meyer, S., Schelbert, S., Schneider, T., Weschke, W., Peters, S. W., Keller, F.,**
548 **Baginsky, S., Martinoia, E., & Schmidt, U. G.** (2006). Identification of a vacuolar sucrose
549 transporter in barley and arabidopsis mesophyll cells by a tonoplast proteomic approach.
550 *Plant Physiology*, *141*(1), 196–207. https://doi.org/10.1104/pp.106.079533
551 **Erilova, A., Brownfield, L., Exner, V., Rosa, M., Twell, D., Scheid, O. M., Hennig, L., & Köhler, C.**
552 (2009). Imprinting of the Polycomb group gene MEDEA serves as a ploidy sensor in
553 Arabidopsis. *PLoS Genetics*, *5*(9). https://doi.org/10.1371/journal.pgen.1000663
554 **Feng, C., Roitinger, E., Hudecz, O., Cuacos, M., Lorenz, J., Schubert, V., Wang, B., Wang, R.,**
555 **Mechtler, K., Heckmann, S.** (2023). TurboID-based proteomic profiling of meiotic
556 chromosome axes in Arabidopsis thaliana. Nat. Plants. 9, 616-630
557 **Geldner, N., Dénervaud-Tendon, V., Hyman, D.L., Mayer, U., Stierhof, Y.D., Chory, J.** (2009).
558 Rapid, combinatorial analysis of membrane compartments in intact plants with a
559 multicolor marker set. Plant J.;59(1):169-78. PMID: 19309456
560 **Geldner, N., Anders, N., Wolters, H., Keicher, J., Kornberger, W., Muller, P., Delbarre, A., Ueda,**
561 **T., Nakano, A., Jurgens, G.** (2003). The Arabidopsis GNOM ARF-GEF mediates endosomal
562 recycling, auxin transport, and auxin-dependent plant growth. *Cell* **112**: 219-230
563 **Jürgens, G.** (2005). Plant cytokinesis: Fission by fusion. *Trends in Cell Biology*, *15*(5), 277–283.
564 https://doi.org/10.1016/j.tcb.2005.03.005
565 **Kanazawa, T., Ueda, T.** (2017). Exocytic trafficking pathways in plants: why and how they are
566 redirected. *New Phytologist,* 215: 952-957
567 **Kim, D. Y., Hong, M. J., & Seo, Y. W.** (2019). Genome-wide transcript analysis of inflorescence
568 development in wheat. *Genome*, *62*(9), 623–633. https://doi.org/10.1139/gen-2018-0200
569 **Kradolfer, D., Wolff, P., Jiang, H., Siretskiy, A., & Köhler, C.** (2013). An imprinted gene underlies
570 postzygotic reproductive isolation in arabidopsis thaliana. *Developmental Cell*, *26*(5), 525–
571 535. https://doi.org/10.1016/j.devcel.2013.08.006
572 **Lei, X., Ning, Y., Elesawi, I. E., Yang, K., Chen, C., & Liu, B.** (2020). Heat stress interferes with
573 chromosome segregation and cytokinesis during male meiosis in Arabidopsis thaliana.

Plant Signaling & Behavior, *15*(5). https://doi.org/10.1080/15592324.2020.1746985

Leshem, Y., Seri, L., Levine, A. (2007). Induction of phosphatidylinositol 3-kinase-mediated endocytosis by salt stress leads to intracellular production of reactive oxygen species and salt tolerance. *Plant J* **51**: 185-197

Lukowitz, W., Gillmor, C. S., & Scheible, W.-R. R. (2000). Positional cloning in Arabidopsis. Why it feels good to have a genome initiative working for you. *Plant Physiology*, *123*(3), 795–805. https://doi.org/10.1104/pp.123.3.795

Ovečka, M., Vaškebová, L., Komis, G., Luptovčiak, I., Smertenko, A., Šamaj, J. (2015). Preparation of plants for developmental and cellular imaging by light-sheet microscopy. Nat. Protoc. 10, 1234–1247

Ramsey, J., & Schemske, D. W. (1998). Pathways, mechanisms, and rates of polyploid formation in flowering plants. *Annual Review of Ecology and Systematics*, *29*, 467–501. https://doi.org/10.1146/annurev.ecolsys.29.1.467

Reichardt, I., Stierhof, Y. D., Mayer, U., Richter, S., Schwarz, H., Schumacher, K., & Jürgens, G. (2007). Plant Cytokinesis Requires De Novo Secretory Trafficking but Not Endocytosis. *Current Biology*, *17*(23), 2047–2053. https://doi.org/10.1016/j.cub.2007.10.040

Renault, L., Christova, P., Guibert, B., Pasqualato, S., Cherfils, J. (2002). Mechanism of domain closure of Sec7 domains and role in BFA sensitivity. *Biochemistry* **41**: 3605-3612.

Richter S, Schrader J, Wolters H, Stierhof YD, Rios G, Koncz C, Robinson DG, Jürgens G. (2007). Functional diversification of closely related ARF-GEFs in protein secretion and recycling. *Nature*, 448, 488-492

Rodkiewicz, B. & Duda, E. (1988). Aggregations of organelles in meiotic cells of higher plants. Acta Soc Bot Pol 57(4):637–654

Segui-Simarro. JM., Staehelin, L. A. (2006). Cell cycle-dependent changes in Golgi stacks, vacuoles, clathrin-coated vesicles and multivesicular bodies in meristematic cells of Arabidopsis thaliana: a quantitative and spatial analysis. *Planta* 223: 223-236

Shimaoka, T., Ohnishi, M., Sazuka, T., Mitsuhashi, N., Hara-Nishimura, I., Shimazaki, K. I., Maeshima, M., Yokota, A., Tomizawa, K. I., & Mimura, T. (2004). Isolation of intact vacuoles and proteomic analysis of tonoplast from suspension-cultured cells of Arabidopsis thaliana. *Plant and Cell Physiology*, *45*(6), 672–683. https://doi.org/10.1093/pcp/pch099

Tchórzewska, D. (2017). Chondriokinesis during microsporogenesis in plants. *Planta*, *246*(1), 1–18. https://doi.org/10.1007/s00425-017-2706-8

Teh OK, Moore I. (2007). An ARF-GEF acting at the Golgi and in selective endocytosis in polarized plant cells. *Nature*, 448, 493-496

Valuchova, S., Mikulkova, P., Pecinkova, J., Klimova, J., Krumnikl, M., Bainar, P., Heckmann, S., Tomancak, P., Riha, K. (2020). Imaging plant germline differentiation within Arabidopsis flowers by light sheet microscopy. eLife 9, e52546

611 **Van Damme, D., Inze, D., Russinova, E.** (2008). Vesicle trafficking during somatic cytokinesis.
612 *Plant Physiol* **147**: 1544-1552
613 **Yi, J., Kradolfer, D., Brownfield, L., Ma, Y., Piskorz, E., Köhler, C., & Jiang, H.** (2023). Meiocyte
614 size is a determining factor for unreduced gamete formation in Arabidopsis thaliana. *New*
615 *Phytologist*, *237*(4), 1179–1187. https://doi.org/10.1111/nph.18473
616 **Zhang, Y. N., Wei, D. M., Song, Y. Y., Chen, L., Zhu, X. Y., & Tian, H. Q.** (2011). Microtubule
617 organization during successive microsporogenesis in Allium cepa and simultaneous
618 cytokinesis in Nicotiana tabacum. *Biologia Plantarum*, *55*(4), 752–756.
619 https://doi.org/10.1007/s10535-011-0181-9
620 **Zhang, L., Xing, J., Lin. J.** (2019). At the intersection of exocytosis and endocytosis in plants. *New*
621 *Phytologist* **224**: 1479-1489

622

623 **Acknowledgements**
624 We gratefully acknowledge Amanda Souza Camara for her expert assistance with the protein
625 interaction analysis using AlphaFold2, and Markus Grebe for his valuable feedback that helped
626 improve the manuscript. This research was supported by intramural funding from Leibniz Institute
627 of Plant Genetics and Crop Plant Research (IPK), Gatersleben (to HJ), and a grant from the German
628 Research Foundation (DFG) to HJ (JI 347/5-1).

629

630 **Author contributions**

631 E.P., Y.M., and H.J. conceived and designed the experiments, and wrote the manuscript. J.Y. and
632 M.C. executed the experimental procedures. D.K. and C.K. contributed materials. All authors
633 discussed the results and commented on the manuscript.

634

635 **Competing interests**

636 The authors declare no competing interests.

637

638 **Figure legends**

639 **Figure 1.** Phenotypic analysis of *jas pele*. (A) Photographs of pollen. Red asterisks indicate diploid
640 pollen. Scale bar, 50 µm. (B) Box plot showing the distribution of pollen size in WT, *jas*, and *jas*
641 *pele*. The lower and upper hinges of the boxplots correspond to the first and third quartiles of the
642 data, the black lines within the boxes mark the median, whiskers represent Minimum and

643 Maximum, and circles represent outliers. Asterisks mark significance (Kolmogorov–Smirnov test,
644 $P < 10^{-5}$). Numbers above indicate the number of meiotic products observed.(C) Photographs of
645 meiotic products stained with toluidine blue. From left to right: tetrad, triad, dyad. Scale bar, 10
646 µm. Numbers above indicate number of meiotic products observed. (D) Analysis of tetrad
647 formation, with the number of analyzed meiotic products indicated above.E) Tetrad formation of
648 *osd1*, *ps1*, and their progeny from crosses with *pele* and/or *jas*. Significance of the differences was
649 tested by Chi-square test. Asterisks mark significance ($P < 10^{-5}$), ns, not significant. Numbers
650 above indicate the number of meiotic products observed.

651 **Figure 2.** Meiotic progression in *jas pele*. (A) Chromosome spreads of wild-type (WT), *jas,* and *jas*
652 *pele* meiocytes. Scale bars, 10 µm. (B) Microtubule dynamics during meiosis in WT, *jas*, and *jas*
653 *pele.* Green signals are from the microtubular cytoskeleton, and red (false color) signals are
654 chromosomes. Very faint or no red signals in some images are due to weak DAPI staining. Scale
655 bars, 5 µm.

656 **Figure 3.** Organelle band types. (A–C) Analysis of whole anthers at metaphase II in WT (A), *jas* (B),
657 and *jas pele* (C), highlighting the three types of organelle bands observed (arrows). Scale bar, 10
658 µm. (D) Percentage distribution of metaphase II meiocytes with complete, partial, or absent
659 organelle bands observed in WT, *jas*, and *jas pele*. Significance of the differences was tested by
660 Chi-square test. Asterisks mark significance ($P <10^{-5}$), ns, not significant. Numbers above indicate
661 the number of meiotic cells observed. (E) Localization of the makers of the plasma membrane
662 (PM), PIP1;4, and trans-Golgi network (TGN), VTI12, in defined genotypes. Scale bar, 10 µm. (F)
663 Box plot showing the distribution of distance between two groups of chromosomes at metaphase
664 II. The lower and upper hinges of the boxplots correspond to the first and third quartiles of the
665 data, the black lines within the boxes mark the median, whiskers represent Minimum and
666 Maximum, and circles represent outliers. Asterisks mark significance (Kolmogorov–Smirnov test,
667 $P <10^{-5}$). Numbers above indicate the number of meiotic products observed. (G) Localization of
668 PM and TGN markers in meiocytes at the metaphase II stage in WT, *jas*, and *jas pele*.

669 **Figure 4.** The effect of vesicle trafficking inhibitors on meiosis in the mutants. The effect of vesicle
670 trafficking inhibitors on meiosis in the mutants. (A) Analysis of tetrad formation in WT, *jas*, and
671 *jas pele* after subjecting the inflorescences to Concanamycin A (ConA), and the control DMSO.
672 Numbers above indicate the number of meiotic products observed. (B) Analysis of tetrad
673 formation in WT, *jas*, and *jas pele* after subjecting the inflorescences to Brefeldin A (BFA), and
674 Wortmannin (Wort), and the control DMSO. Numbers above indicate the number of meiotic
675 products observed. (C) Percentage distribution of metaphase II meiocytes with complete, partial,
676 or absent organelle bands observed in *jas pele* after subjecting the inflorescences to vesicle
677 trafficking inhibitors. Significance of the differences was tested by Chi-square test. Asterisks mark
678 significance ($P <10^{-5}$), ns, not significant. Numbers above indicate the number of meiotic cells

679 observed. (D) Box plots showing the distribution of distance between two groups of
680 chromosomes at metaphase II in BFA, Wortmannin, and DMSO-treated *jas pele*. The lower and
681 upper hinges of the boxplots correspond to the first and third quartiles of the data, the black lines
682 within the boxes mark the median, whiskers represent Minimum and Maximum, and circles
683 represent outliers. Asterisks mark significance (Kolmogorov–Smirnov test, $P < 10^{-5}$). Numbers
684 above indicate the number of meiotic cells observed.

685 **Figure 5.** PELE localization in meiocytes and roots. (A) Localization of PELE-GFP at metaphase II in
686 WT meiocytes. Green signals are from PELE-GFP, red signals are from chromosomes. Scale bar,
687 10 µm. (B) Localization of PELE-GFP in roots. RabG3F, late endosome and tonoplast; VAMP711,
688 tonoplast. Scale bar, 5 µm.

689 **Figure 6.** Function of UBQL in organelle band regulation. (A) Predicted protein interaction
690 between PELE and UBQL using AlphaFold2. UBQL is shown in yellow, and PELE is shown in purple.
691 (B) Magnified image of the protein interaction site in (A). Polar bonds are indicated by red dotted
692 lines. (C) Yeast two-hybrid assay results showing interaction between UBQL and the PELE (909-
693 1296) fragment. (D) Analysis of tetrad formation in WT, *jas*, *jas ubql*, *jas pele*, and *jas pele ubql*
694 mutants. Numbers above indicate the number of meiotic products observed. (E) Predicted
695 percentage distribution of haploid and diploid pollen based on the tetrad analysis results in (D).
696 Statistical significance was tested using the Chi-square test. Asterisks indicate significant
697 differences ($P < 10^{-5}$); ns, not significant. Numbers above indicate the number of meiotic products
698 observed. (F) Violin plots showing the distribution of the distance between two chromosome
699 groups at metaphase II in WT, *jas*, *jas ubql*, *jas pele*, and *jas pele ubql*. The lower and upper hinges
700 of the boxplots correspond to the first and third quartiles of the data. The black lines within the
701 boxes represent the median, whiskers represent the minimum and maximum values, and circles
702 represent outliers. Asterisks indicate significant differences (Kolmogorov–Smirnov test, $P < 10^{-5}$).
703 Numbers above indicate the number of meiotic cells observed.

704 **Figure 7.** Model of secretory trafficking in organelle band organization. The figure illustrates how
705 the balance between PELE-UBQL and JAS regulates the transport of proteins and membrane
706 components to both the organelle band and the vacuole. PELE and UBQL exhibit an antagonistic
707 interaction that refines the trafficking pathway towards the vacuole. Disruption in JAS, PELE, or
708 UBQL causes an imbalance in this regulatory system, leading to altered secretory trafficking and
709 affecting the organization of the organelle band.
710

711

712 **Supplemental figure legends**

713 **Figure S1.** Confirmation of the point mutation within AT5G11700. (A) dCAPS analysis of the point
714 mutations in *jas-3* and *jas-3 pele*. (B) PCR product sequencing confirming the point mutation in
715 AT5G11700, which results in the generation of a stop codon. (C) Analysis of tetrad formation in
716 six representative *jas-3* at5g11700 double mutants. The number of analyzed meiotic products is
717 indicated above the bars.

718 **Figure S2.** Phenotypic analysis of the *pele* single mutant. (A) Distribution of pollen size in the *pele*
719 single mutant and three control lines. (B) Percentage of meiotic products in *pele* and the control
720 lines. (C) Stages of meiosis in *pele*; from left to right: diakinesis, metaphase I, anaphase I, prophase
721 II, metaphase II, anaphase II, telophase II, and the four nuclei stage. Scale bar is 10 µm, which is
722 identical to all photos.

723 **Figure S3.** Structure of PELE and histochemical GUS staining in tissues of Pro:PELE-GUS plants. (A)
724 Schematic representation of the PELE protein structure predicted by SMART (embl-
725 heidelberg.de). The diagram includes the T-DNA insertion site and most commonly predicted
726 features, such as the four transmembrane domains and the cleavable signal peptide at the N
727 terminus. The amino acid with a point mutation in the *pele* mutant is indicated by a lightning
728 mark. (B–G) Histochemical GUS staining in tissues of Pro:PELE-GUS plants. (B) 7-day-old seedling.
729 (C) 7-day-old seedling, with more visible staining in the root. (D) 14-day-old seedling. (E) Top of a
730 leaf of a 4-week-old plant. (F) Cauline leaf of a 5-week-old plant. (G) Inflorescence of a 5-week-
731 old plant. Scale bars, 1 mm.

732 **Figure S4.** PELE localization with organelle markers in roots. NIP1, ER and the plasma membrane;
733 Got1p homolog, the Golgi apparatus; VTI12, the trans-Golgi-network and early endosome;
734 RabF2a, late endosome and pre-vacuolar compartment. Scale bar, 5 µm.
735
736 **Table S1** Complementation analysis for *jas pele*.
737
738 **Table S2** Primers used in the manuscript.

Figure 1

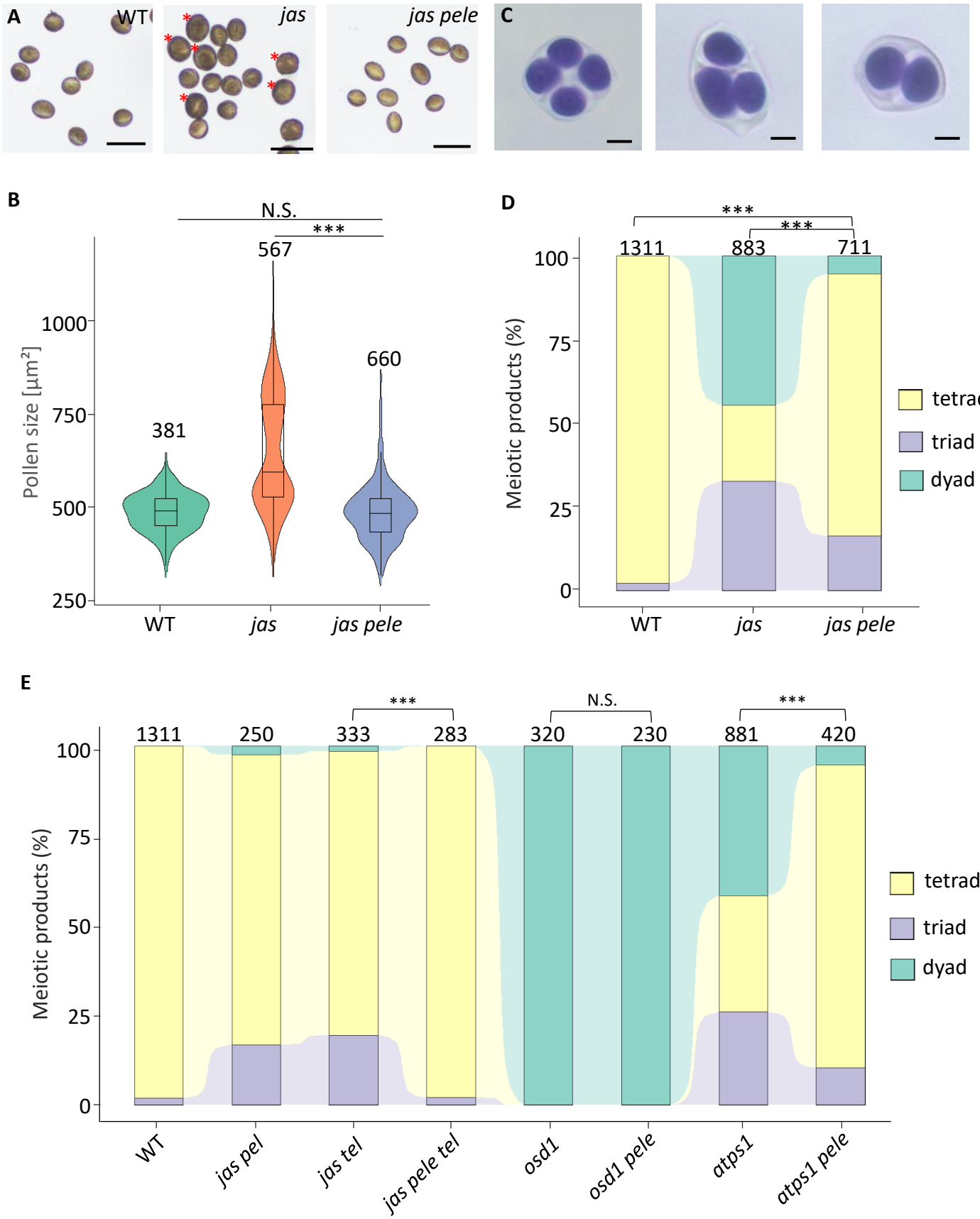
A
WT
jas
jas pele
C
B
N.S.
***
567
660
381
1000
750
500
250
Pollen size [µm²]
WT
jas
jas pele
D
***
***
1311
883
711
100
75
50
25
0
Meiotic products (%)
tetrad
triad
dyad
WT
jas
jas pele
E
***
N.S.
***
1311
250
333
283
320
230
881
420
100
75
50
25
0
Meiotic products (%)
tetrad
triad
dyad
WT
jas pel
jas tel
jas pele tel
osd1
osd1 pele
atps1
atps1 pele

Figure 1. Phenotypic analysis of *jas pele*. (A) Photographs of pollen. Red asterisks indicate diploid pollen. Scale bar, 50 µm. (B) Box plot showing the distribution of pollen size in WT, *jas*, and *jas pele*. The lower and upper hinges of the boxplots correspond to the first and third quartiles of the data, the black lines within the boxes mark the median, whiskers represent Minimum and Maximum, and circles represent outliers. Asterisks mark significance (Kolmogorov–Smirnov test, $P < 10^{-5}$). Numbers above indicate the number of meiotic products observed.(C) Photographs of meiotic products stained with toluidine blue. From left to right: tetrad, triad, dyad. Scale bar, 10 µm. Numbers above indicate number of meiotic products observed. (D) Analysis of tetrad formation, with the number of analyzed meiotic products indicated above.E) Tetrad formation of *osd1*, *ps1*, and their progeny from crosses with *pele* and/or *jas*. Significance of the differences was tested by Chi-square test. Asterisks mark significance ($P < 10^{-5}$), ns, not significant. Numbers above indicate the number of meiotic products observed.

Figure 2

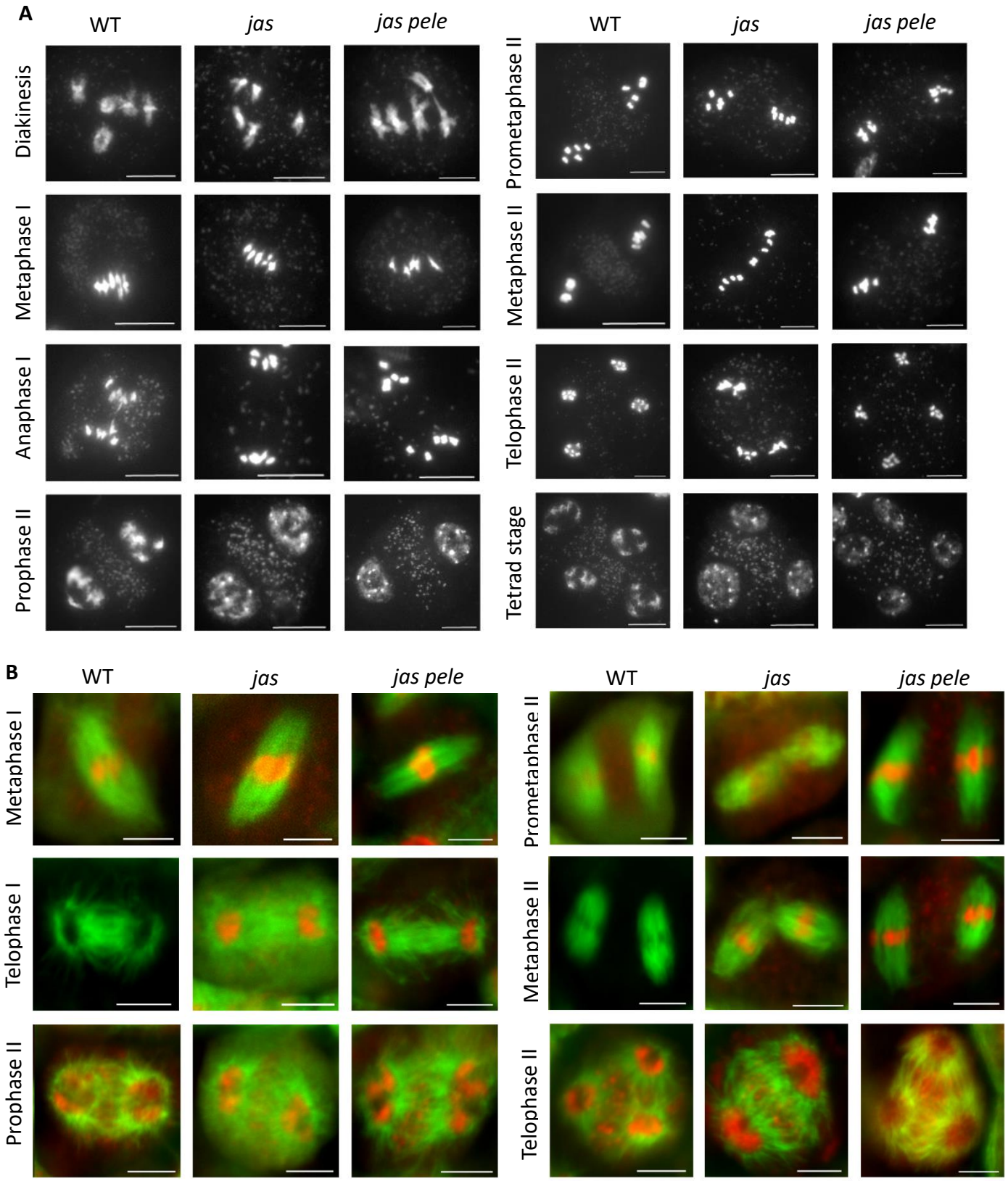

Figure 2 Meiotic progression in *jas pele*. (A) Chromosome spreads showing selected stages of WT, *jas* and *jas pele* meiosis. Scale bar is 10 µm. (B) Microtubules dynamics during selected stages of meiosis in WT, *jas* and *jas pele.* Green is microtubular cytoskeleton, red (false color) are chromosomes. Very faint or no red signals in some images come from weak DAPI staining. Scale bars are 5 µm.

Figure 3

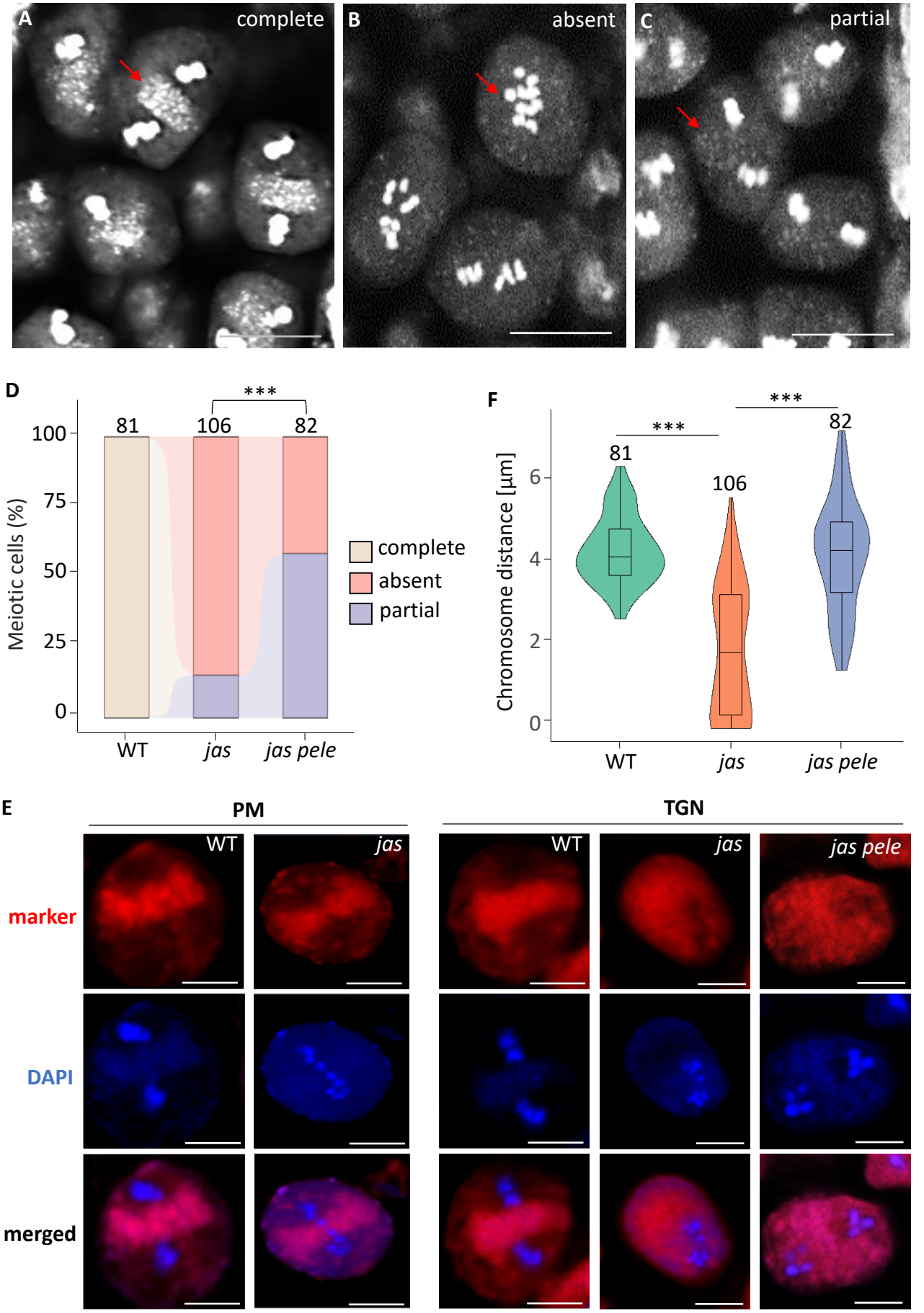
A
complete
B
absent
C
partial
D
***
81
106
82
100
75
50
25
0
Meiotic cells (%)
complete
absent
partial
WT
jas
jas pele
F
***
***
81
106
82
6
4
2
0
Chromosome distance [µm]
WT
jas
jas pele
E
PM
TGN
WT
jas
WT
jas
jas pele
marker
DAPI
merged

Figure 3. Organelle band types. (A–C) Analysis of whole anthers at metaphase II in WT (A), *jas* (B), and *jas pele* (C), highlighting the three types of organelle bands observed (arrows). Scale bar, 10 µm. (D) Percentage distribution of metaphase II meiocytes with complete, partial, or absent organelle bands observed in WT, *jas*, and *jas pele*. Significance of the differences was tested by Chi-square test. Asterisks mark significance ($P < 10^{-5}$), ns, not significant. Numbers above indicate the number of meiotic cells observed. (E) Localization of the makers of the plasma membrane (PM), PIP1;4, and trans-Golgi network (TGN), VTI12, in defined genotypes. Scale bar, 10 µm. (F) Box plot showing the distribution of distance between two groups of chromosomes at metaphase II. The lower and upper hinges of the boxplots correspond to the first and third quartiles of the data, the black lines within the boxes mark the median, whiskers represent Minimum and Maximum, and circles represent outliers. Asterisks mark significance (Kolmogorov–Smirnov test, $P < 10^{-5}$). Numbers above indicate number of meiotic products observed. (G) Localization of PM and TGN markers in meiocytes at the metaphase II stage in WT, *jas*, and *jas pele*.

Figure 4

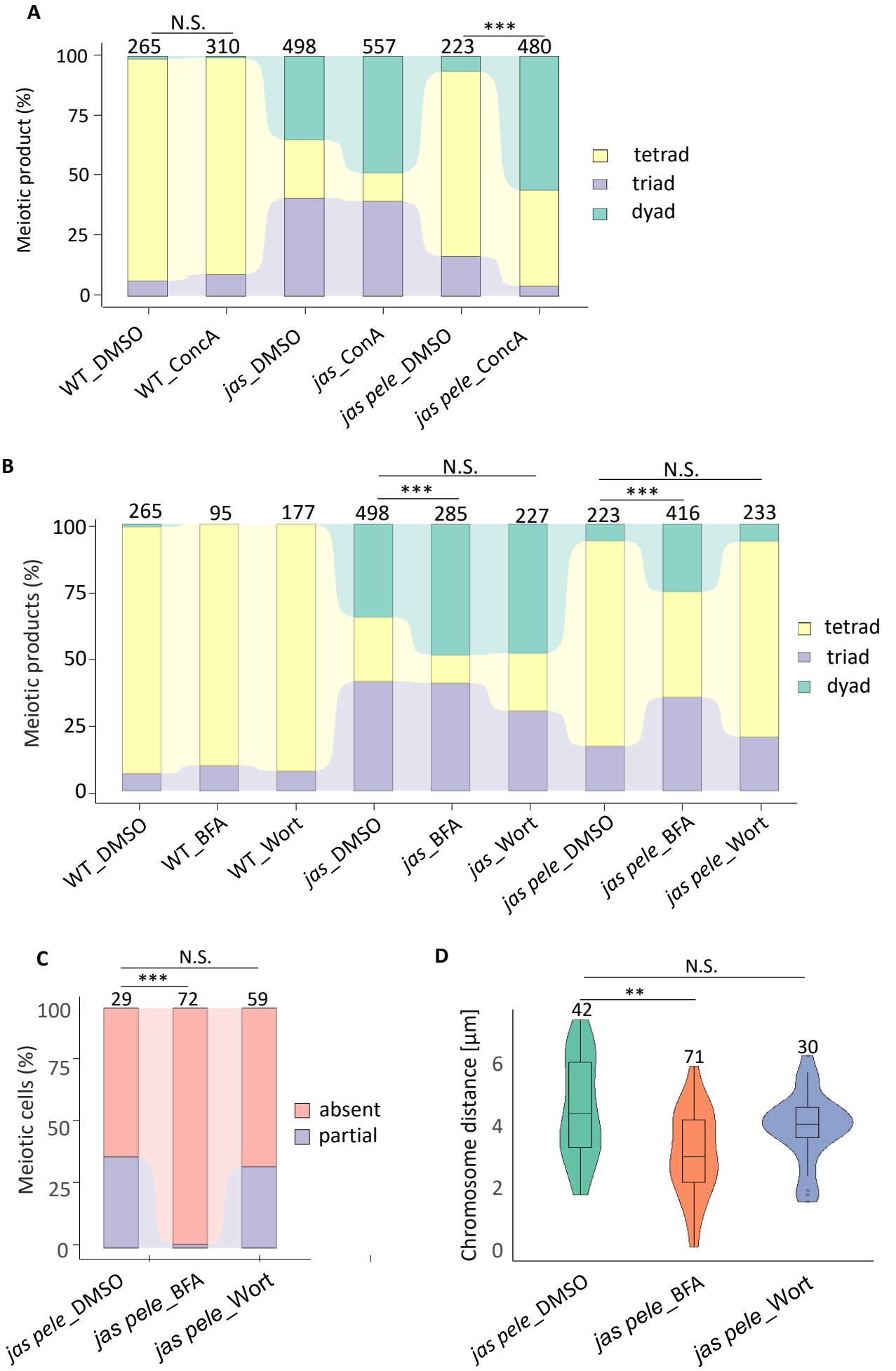
A
N.S.
***
265
310
498
557
223
480
Meiotic product (%)
100
75
50
25
0
tetrad
triad
dyad
WT_DMSO
WT_ConcA
jas_DMSO
jas_ConA
jas pele_DMSO
jas pele_ConcA
B
N.S.
***
N.S.
***
265
95
177
498
285
227
223
416
233
Meiotic products (%)
100
75
50
25
0
tetrad
triad
dyad
WT_DMSO
WT_BFA
WT_Wort
jas_DMSO
jas_BFA
jas_Wort
jas pele_DMSO
jas pele_BFA
jas pele_Wort
C
N.S.
***
29
72
59
Meiotic cells (%)
100
75
50
25
0
absent
partial
jas pele_DMSO
jas pele_BFA
jas pele_Wort
D
N.S.
**
42
71
30
Chromosome distance [µm]
6
4
2
0
jas pele_DMSO
jas pele_BFA
jas pele_Wort

Figure 4. The effect of vesicle trafficking inhibitors on meiosis in the mutants. The effect of vesicle trafficking inhibitors on meiosis in the mutants. (A) Analysis of tetrad formation in WT, *jas*, and *jas pele* after subjecting the inflorescences to Concanamycin A (ConA), and the control DMSO. Numbers above indicate the number of meiotic products observed. (B) Analysis of tetrad formation in WT, *jas*, and *jas pele* after subjecting the inflorescences to Brefeldin A (BFA), and Wortmannin (Wort), and the control DMSO. Numbers above indicate the number of meiotic products observed. (C) Percentage distribution of metaphase II meiocytes with complete, partial, or absent organelle bands observed in *jas pele* after subjecting the inflorescences to vesicle trafficking inhibitors. Significance of the differences was tested by Chi-square test. Asterisks mark significance ($P < 10^{-5}$), ns, not significant. Numbers above indicate the number of meiotic cells observed. (D) Box plots showing the distribution of distance between two groups of chromosomes at metaphase II in BFA, Wortmannin, and DMSO-treated *jas pele*. The lower and upper hinges of the boxplots correspond to the first and third quartiles of the data, the black lines within the boxes mark the median, whiskers represent Minimum and Maximum, and circles represent outliers. Asterisks mark significance (Kolmogorov–Smirnov test, $P < 0.01$). Numbers above indicate the number of meiotic cells observed.

Figure 5

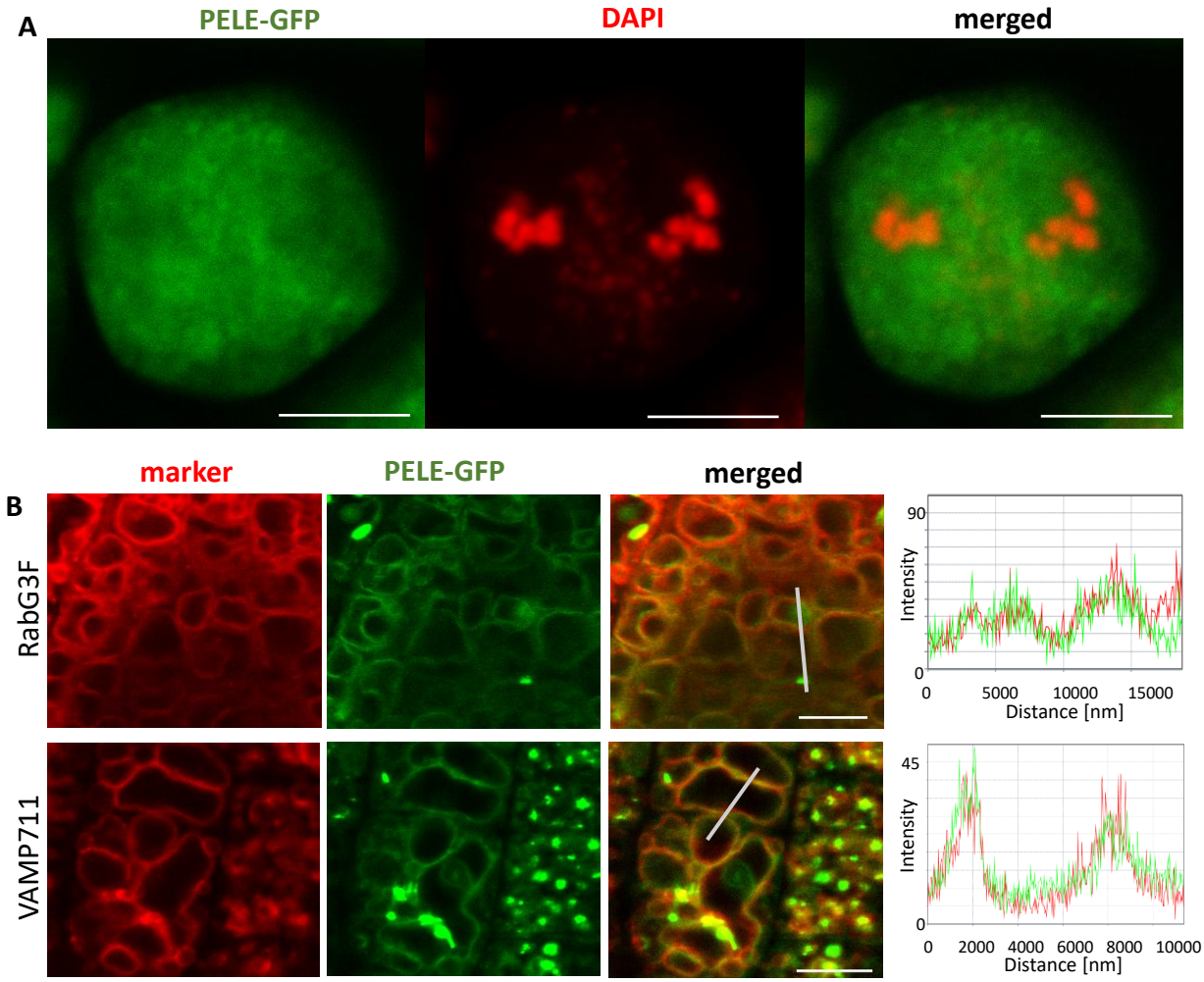

Figure 5. PELE localization in meiocytes and roots. (A) Localization of PELE-GFP at metaphase II in WT meiocytes. Green signals are from PELE-GFP, red signals are from chromosomes. Scale bar, 10 µm. (B) Localization of PELE-GFP in roots. RabG3F, late endosome; VAMP711, tonoplast. Scale bar, 5 µm.

Figure 6

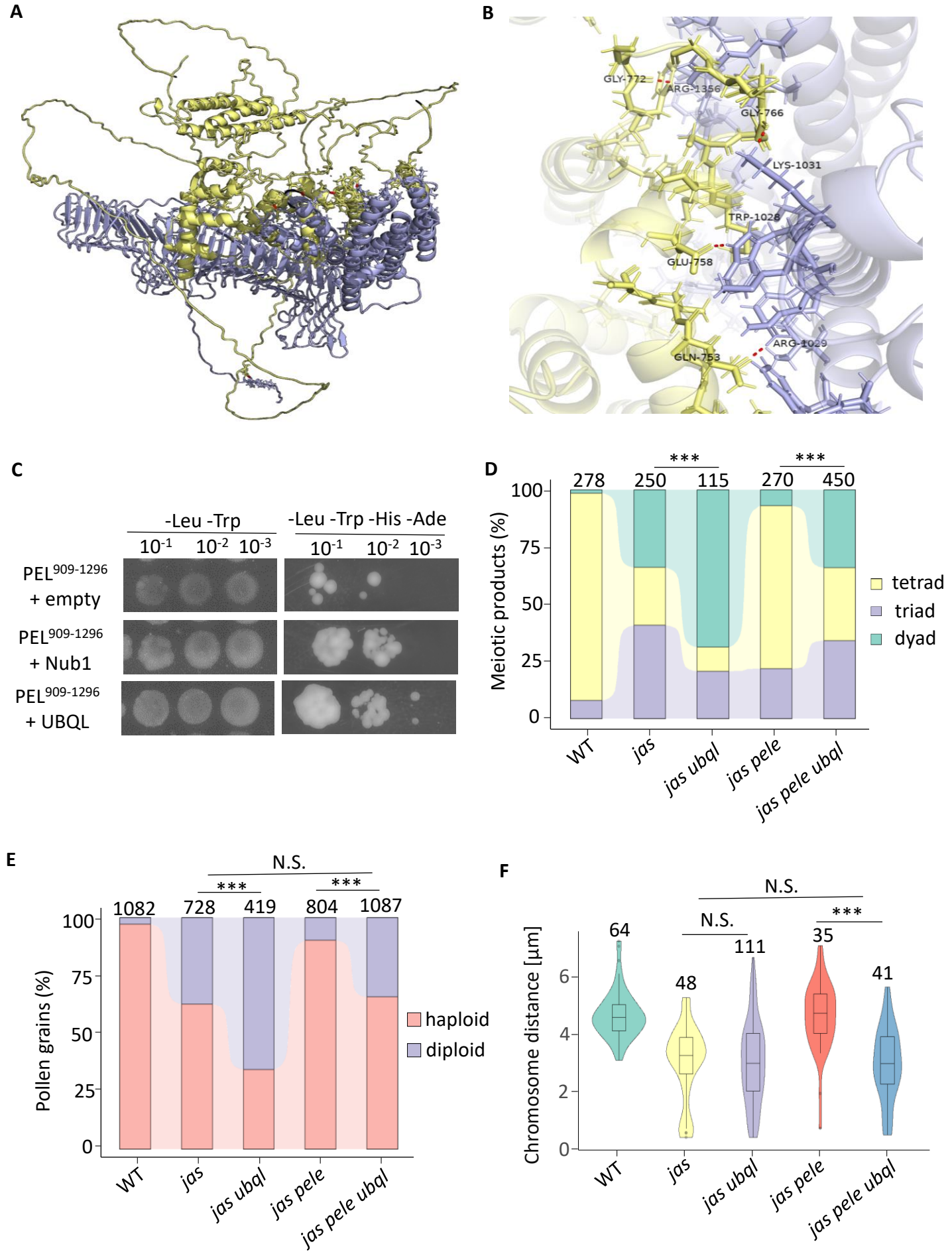
A
B
GLY-772
ARG-1356
GLY-766
LYS-1031
TRP-1028
GLU-758
ARG-1029
GLN-753
C
-Leu -Trp
-Leu -Trp -His -Ade
10-1 10-2 10-3
PEL909-1296 + empty
PEL909-1296 + Nub1
PEL909-1296 + UBQL
D
Meiotic products (%)
278 250 115 270 450
***
***
tetrad
triad
dyad
WT
jas
jas ubql
jas pele
jas pele ubql
E
Pollen grains (%)
1082 728 419 804 1087
N.S.
***
***
haploid
diploid
WT
jas
jas ubql
jas pele
jas pele ubql
F
Chromosome distance [µm]
64 48 111 35 41
N.S.
N.S.
***
WT
jas
jas ubql
jas pele
jas pele ubql

Figure 6. Function of UBQL in organelle band regulation. (A) Predicted protein interaction between PELE and UBQL using AlphaFold2. UBQL is shown in yellow, and PELE is shown in purple. (B) Magnified image of the protein interaction site in (A). Polar bonds are indicated by red dotted lines. (C) Yeast two-hybrid assay results showing interaction between UBQL and the PELE (909-1296) fragment. (D) Analysis of tetrad formation in WT, *jas*, *jas ubql*, *jas pele*, and *jas pele ubql* mutants. Numbers above indicate the number of meiotic products observed. (E) Predicted percentage distribution of haploid and diploid pollen based on the tetrad analysis results in (D). Statistical significance was tested using the Chi-square test. Asterisks indicate significant differences ($P < 10^{-5}$); ns, not significant. Numbers above indicate the number of meiotic products observed. (F) Violin plots showing the distribution of the distance between two chromosome groups at metaphase II in WT, *jas*, *jas ubql*, *jas pele*, and *jas pele ubql*. The lower and upper hinges of the boxplots correspond to the first and third quartiles of the data. The black lines within the boxes represent the median, whiskers represent the minimum and maximum values, and circles represent outliers. Asterisks indicate significant differences (Kolmogorov–Smirnov test, $P < 10^{-5}$). Numbers above indicate the number of meiotic cells observed.

Figure 7

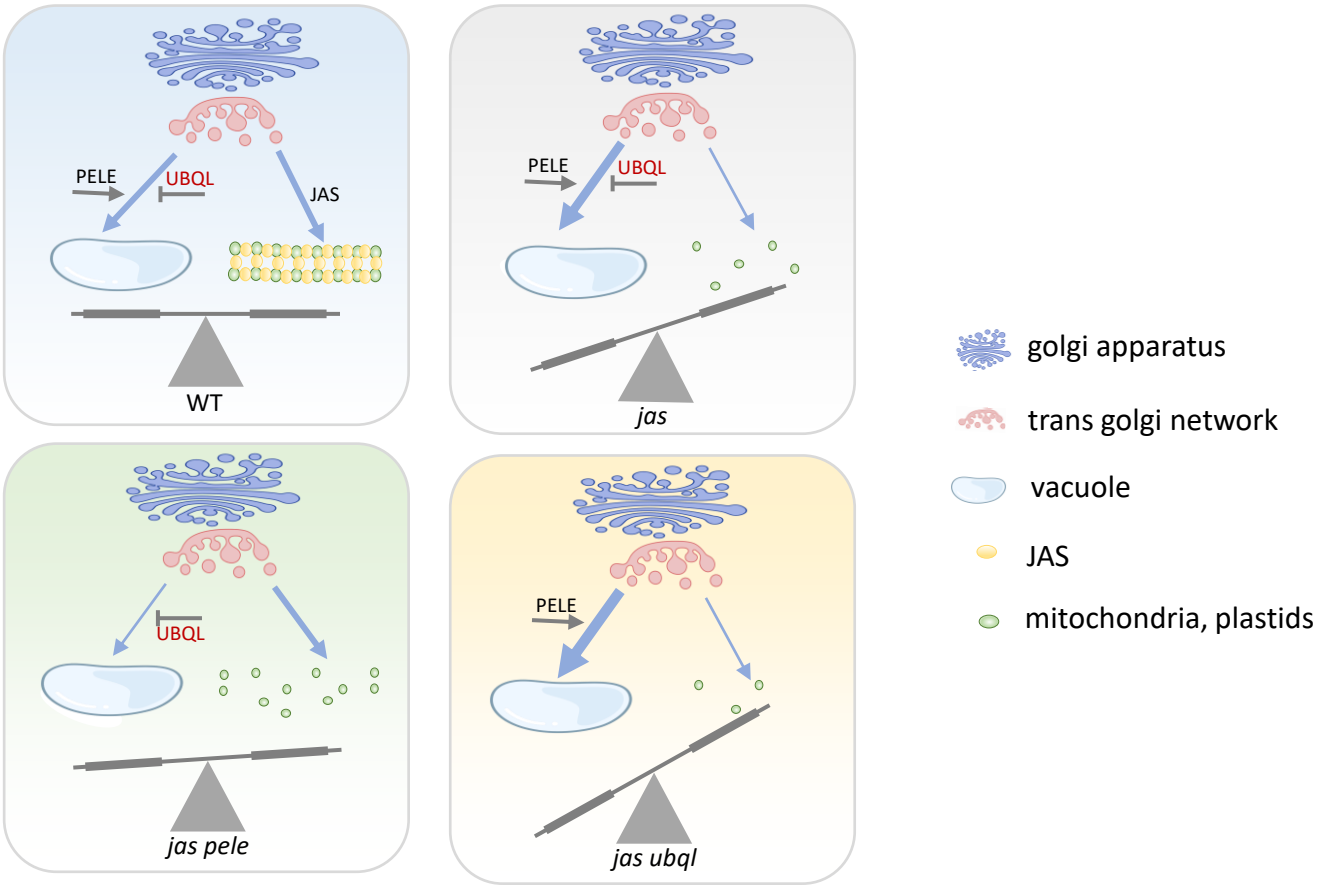

Figure 7. Model of secretory trafficking in organelle band organization. The figure illustrates how the balance between PELE-UBQL and JAS regulates the transport of proteins and membrane components to the organelle band and the vacuole. PELE and UBQL exhibit an antagonistic interaction that refines the trafficking pathway towards the vacuole. Disruption in JAS, PELE, or UBQL causes an imbalance in this regulatory system, leading to altered secretory trafficking and affecting the organization of the organelle band.